Anisotropic Conductivity of Rat Head Phantom and Its Influence on Electroencephalogram Source Localization

**JAROSLAV LACIK[1], (Member, IEEE), VLASTIMIL KOUDELKA[2], CESTMIR VEJMOLA[2,3],
DAVID KURATKO[1], JIRI VANEK[1], DANIEL KRZYSZTOF WÓJCIK[1,4], TOMAS PALENICEK[2,3],
AND ZBYNEK RAIDA[1], (Senior Member, IEEE)**

[1]Faculty of Electrical Engineering and Communication, Brno University of Technology, 61600 Brno, Czech Republic
[2]National Institute of Mental Health, 25067 Klecany, Czech Republic
[3]Third Faculty of Medicine, Charles University, 10000 Prague, Czech Republic
[4]Nencki Institute of Experimental Biology of Polish Academy of Sciences, 02-093 Warsaw, Poland

Corresponding authors: Jaroslav Lacik (lacik@vut.cz) and Vlastimil Koudelka (vlastimil.koudelka@nudz.cz)

ABSTRACT In this paper we deal with a simplified anisotropic rat head phantom development and the investigation of the influence of the anisotropic white matter on electroencephalogram source localization. The proposed phantom is based on the cubic cross cell composition combined with agar mixture to set desired electrical conductivity anisotropic ratio. For the fabrication of the phantom, the 3D printed technology is exploited. Starting from a real rat brain, we proposed a simplified brain model incorporating the actual dimensions, shape and conductivity parameters of both grey and white matter containing simultaneously relevant deep-brain electrical signal sources. Five testing dipoles were located in the areas corresponding to the active brain regions. A single dipole localization error was calculated by comparing an inverse solution with a dipole position obtained from a computer tomography image. Neglecting anisotropy had a rather weak effect on localization error of a single testing dipole in our model. The reliability map was computed and interpreted in terms of spatial similarity between distributed inverse solutions involving isotropic and anisotropic forward models. We found spatially specific error increases located close to the electrodes and in the vicinity of anisotropic compartment. Hence, areas to be most sensitive to neglecting anisotropy in our model were identified.

INDEX TERMS Rat head phantom, electroencephalogram, source localization, white matter anisotropic conductivity, conductivity measurement, agar, 3D printing.

I. INTRODUCTION

The electroencephalogram (EEG) source localization is an important tool for (pre)clinical and basic brain research. Its goal is to find positions of active brain areas from EEG signals measured on the brain/head surface. It consists of forward and inverse problems. The forward problem deals with evaluation of the potential on the head surface for known positions of electric sources usually modeled by electric current dipoles located inside the brain [1]. The inverse problem exploits the forward model to reconstruct position of active brain areas from the potentials measured on the head surface. The

The associate editor coordinating the review of this manuscript and approving it for publication was Junhua Li.

accuracy of the solution depends on different factors, such as the number and distribution of EEG electrodes, signal to noise ratio, used inverse technique and the accuracy of the forward problem solution.

In past decades, lots of effort has been devoted to the development of head models, and investigation concentrated on the influence of simplified head models on the accuracy of forward and inverse procedure. Those head models range from the simple single sphere to the realistic one developed exploiting magnetic resonance (MR) or computed tomography (CT) data allowing segmentation head tissue types. The earliest investigated models have been based on the assumption of isotropic electric conductivity of head tissues. However, head tissues exhibit anisotropic behavior [2]–[4].

Thus, the various investigations have been carried out mainly on human head models to study the effects of anisotropic tissues on the forward and inverse solution.

For a robust cortical source localization procedure, it was recommended considering a realistic head model taking anisotropy of tissues into account [3]. In [5] it was observed that the skull anisotropy has a smearing effect on the forward potential computation. However, in [6] it was reported that the skull geometry simplification has a larger effect on source localization than conductivity modelling. The skull should be approximated as accurately as possible and its conductivity should be modeled as isotropic heterogeneous.

In [7] authors investigated the influence of white matter anisotropic conductivity in a rabbit head using both simulations and source localization based on invasive measurements. The results indicated that including of white matter anisotropy information improves accuracy of source localization procedures. However, the influence of anisotropy is more apparent for dipole orientation and magnitude estimation than for dipole localizations. Since the influence of anisotropy on source estimation was found to be complex, the authors warned that a direct transfer of these results to other species has to be carried out with caution. In [8] authors investigated the influence of white matter anisotropic conductivity in a human head. It was reported that including this information is important mainly for highly accurate localization. However, in [9] it was observed that the white matter anisotropic conductivity can have significant influence on source localization procedures especially when the orientation of the test dipole is similar to the orientation of the anisotropic matter. Further, the presented results in [10] show that including white matter anisotropic conductivity improves accuracy of localization procedure of deep sources especially for lower value of a signal to noise ratio.

In [11] the first attempt using a human experimental approach was carried out to investigate the influence of the white matter anisotropic conductivity on the EEG source localization. It was observed that the white matter anisotropic conductivity distributions do not substantially improve the accuracy of EEG dipole localization which is in contrast with the results reported by [9], or [10].

The described anisotropic head tissue investigations, apart from the two works [11] and [7] which dealt with the problem experimentally, were carried out on digital phantoms by a simulations exploiting the finite elements method which is able to deal with anisotropic materials. Unfortunately, for such a digital investigation it is more difficult to take into account motion artifacts, realistic electromagnetic interference (EMI), and to test the EEG measurement system which can be considered by physical phantoms. Although various physical phantoms have been created, e.g. a saline filled tank [12], a human skull phantom [13], mold phantoms based on conductive materials [14], gelatin phantoms [15], [16] and a 3D printed phantom [17], only one [18] is able to mimic skull anisotropy. Unfortunately, there is no physical phantom mimicking the white matter anisotropic conductivity

which could be used to study anisotropy effects on source localization.

The influence of the anisotropic conductivity of head tissues on source localization is still an open issue and considering [7] the investigation should be carried out individually with respect to desired species. Unlike human studies, animal models allow for rigorous experimental control over many variables otherwise unsustainable in humans. Given that the rat is a common model for brain research, we decided (also with respect to our own research goals) to adopt known rat brain parameters to model anisotropy and investigate the influence of the anisotropic white matter of a rat on electroencephalogram source localization.

The organization of the paper is the following. Section II deals with a simplified model of rat head. Section III describes a development of an anisotropic rat head phantom which can be fabricated by a conventional 3D printed technology. Sections IV deals with an investigation focused on the influence of the anisotropic white matter on electroencephalogram source localization and Section V concludes the paper.

II. SIMPLIFIED MODEL OF RAT HEAD

Brain anisotropy is anatomically driven. In a simplified view, brain tissue can be divided into white and grey matter according to their conductivity characteristics. The grey matter represents the neuronal cell bodies, white matter is made up of ordered bundles of axons. While grey matter is considered more or less isotropic, white matter exhibits unambiguously anisotropic properties. The most extensive white matter structures in the rat brain are the corpus callosum, external capsule and so called deep cerebral white matter (Fig. 1). They are clearly visible by all methods of brain imaging, as they run across the whole brain. These structures form a continuous layer of white matter conductively separating the cortex from other subcortical areas [19].

For the determination of brain parameters, we relied mainly on Diffusion Tensor Imaging (DTI) studies. DTI allows for the measurement of microstructural characteristics of tissue. It provides a representation of the local water diffusion properties in the tissue in a directionally-dependent manner, thus quantifying this level of directional dependency or anisotropy [20], [21]. This is particularly useful in the brain where white matter has typically a highly preferential diffusion direction (i.e. more diffusion along the axons rather than perpendicular to them). Indices commonly derived from DTI include (1) mean diffusivity, independent of direction; (2) fractional anisotropy, quantifying the level of directional dependency; (3) axial diffusivity, parallel component of the amount of diffusion; and (4) radial diffusivity, perpendicular component of the amount of diffusion. In cerebral white matter, contributions to these indices come from fiber arrangements, degree of myelination, and axonal integrity [22]. In most white matter, the diffusivity is anisotropic. Areas of anisotropic diffusivity are seen in Fig. 1 in bright shade (most visible are corpus callosum and external capsule). These are

usually heavily myelinated or densely packed and coherently organized axons. The white matter of the rat is dispersively anisotropic in all directions. However, in the corpus callosum region, lateral (horizontal, x) directionality clearly predominates, while in the regions of the external capsule and deep cerebral white matter, diffusivity is most pronounced in the dorsoventral axis (vertical, z) [23].

To design phantom dimensions, we simplified the rat brain to a right square prism of dimensions $15 \times 15 \times 10$ mm. The ratios of the side lengths were adopted from the actual dimensions of the rat brain while omitting the olfactory bulbs and cerebellum (Fig. 1). The main white matter mass of the rat brain was simplified to a three-dimensional inverted-U shape object. It was designed to maximally preserve the parameters of rat brain white matter in its dimensions (corresponding to the average width of this layer 0.4 mm), its conductivity and preferred direction. Fig. 1 represents the initial anatomical template (Fig. 1(a), Fig. 1(b)) and a sketch of the phantom with parameters adopted from this template (Fig. 1(c), Fig. 1(d)). While compromising anatomical and technical compliancies, we have established 5 distinct excitation dipoles located in a geometrically regular rectangle arrangement mimicking real sources of deep brain signal. We placed dipoles in the specified regions of interest. Four are located symmetrically at the marginals of the quadrants of major subcortical regions representing the basal ganglia and hippocampus. Fifth dipole was placed at the center of the base of the brain, representing the thalamus. We placed 15 sensing electrodes on the outer surface of the phantom, embedded

with their tails in the plastic chassis of the model so that they were aligned with its inner edge, which is in parallel with our surgical procedures in animal models. Nine electrodes were placed in a regular grid on the upper surface of the phantom, 3 electrodes were placed on the left side wall, 3 electrodes and the ground electrode (GND) were placed on the front side wall of the phantom. Fig. 1 represents the initial anatomical template for designing phantom and also depicts the eventual corresponding locations of dipoles in the rat brain according to the phantom model.

Conductivity for the isotropic part of the phantom was established as 0.33 S/m which is the conventional value used for brain modelling [8]. Desired anisotropic ratio of the electric conductivity was set to 10 [5]. In order to define conductivity values within the anisotropic layer the Wang condition described in [5] was applied. This resulted in the following conductivity values for the horizontal anisotropic layer of the inverted-U shape white matter approximation: $\sigma_{xx} = 1.04$ S/m, $\sigma_{yy} = 0.104$ S/m, and $\sigma_{zz} = 0.104$ S/m. Similarly we can state for the vertical anisotropic layers of the inverted-U shape: $\sigma_{xx} = 0.104$ S/m, $\sigma_{yy} = 0.104$ S/m, and $\sigma_{zz} = 1.04$ S/m.

III. DEVELOPMENT OF ANISOTROPIC RAT HEAD PHANTOM

In this section we focus on the anisotropic phantom composition which can be fabricated by a conventional 3D printed technology.

A. DESIGN PROCEDURE FOR MIMICKING ANISOTROPIC WHITE MATTER

For mimicking the electromagnetic properties of the anisotropic white matter, we were inspired by [18] where the authors exploited 3D printed layered structure based on a tetrahedral cell having high percentage of free volume filled by a conductive gel to create an anisotropic human head skull. Since the tetrahedral cell shape is unnecessarily complex for our white matter approximation composed of simple blocks, we decided to exploit a cube cross cell (Fig. 2) where the arms of the cross have a square cross-section.
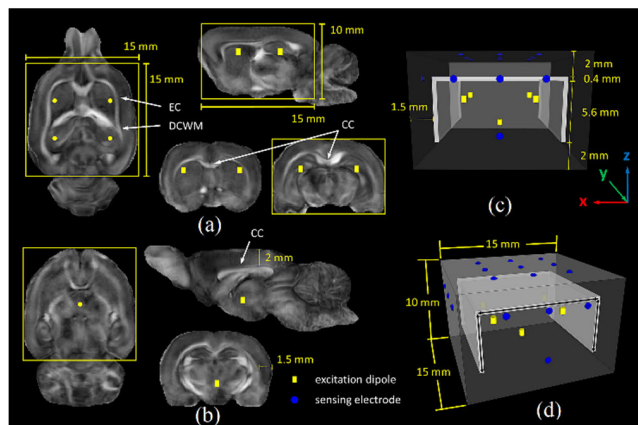

FIGURE 1. Initial schematic of a simplified rat brain model design. (a) and (b), Rat brain DTI atlas (fractional anisotropy) sections (axial, sagittal coronal) corresponding to the plane of locations of the proposed dipoles. Dipoles are indicated by yellow cylinders. The brighter the gray scale, the higher the anisotropic diffusivity. Location of four subcortical dipoles in the quadrants representing basal ganglia and hippocampus (a), a single dipole at the base of the brain representing thalamus (b). CC: corpus callosum, EC: external capsule, DCWM: deep cerebral white matter. Atlas template adopted from [24], created and snapped in ITK-SNAP [25]. (c) and (d), three-dimensional sketch of a right square prism representing a simplified model of a rat brain grey/white matter with dimensions in a scale 1:1. Inverted-U shape in white represents the main mass of the rat brain white matter. The black line terminated by arrows indicates tensors of the white matter anisotropy. Front view (c), view from the upper front left side (d).
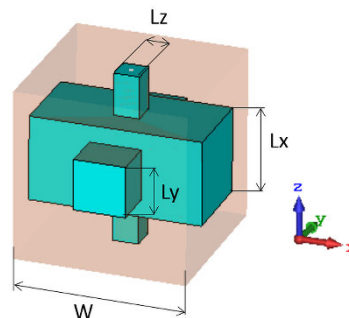

FIGURE 2. A cube cross cell exploited for anisotropic white matter approximation. Arms of the cross have a square cross section.

We can consider the whole cube as a host medium with the electrical conductivity close to zero ($\sigma_h \cong 0$), and the cross is the inclusion with the electrical conductivity much higher than the conductivity of the host medium ($\sigma_i \gg \sigma_h$). Due to the capability of current 3D printed technology, the host medium can be printed and made of plastic, and desired electrical conductivity of the inclusion σ_i can be mimicked by an agar mixture [17].

The effective electrical conductivity of the cell (Fig. 2) can be set by a cross section of a cross arm in a desired direction. Unfortunately, due to the fringing effect of the electric field, a simple formula for their determination based the relation between the resistance R of the constant cross-section cannot be used [26]:

$$R = \frac{l}{\sigma_i A} \qquad (1)$$

where l is the length of the conductor and A is the cross-section area of the conductor. So for the electric conductivity estimation, we decided to exploit the low frequency solver of CST Studio Suite.

Since we consider that the electrical conductivity of the white matter is the same in two directions (e.g. the y and z direction) and different in the third direction (e.g. the x direction), see Section II, we propose a simple design procedure based on the results of the CST Studio Suite where we calculated for given relative dimensions of the arms size of the cross Lx, Ly, and Lz (Fig. 2) to the cube side W (Lx/W, Ly/W, and Lz/W) the resistances R_x and $R_{y,z}$, and consequently corresponding normalized effective conductivities $\sigma_{n\,x}$, and $\sigma_{n\,y,z}$ of such a structure with respect to the relation (1) as follows:

$$\sigma_{n\,x}\left(L_y/W = L_z/W, L_x/W\right) = \frac{1}{R_x W \sigma_i} \qquad (2a)$$

$$\sigma_{n\,y,z}\left(L_x/W, L_y/W = L_z/W\right) = \frac{1}{R_{y,z} W \sigma_i}. \qquad (2b)$$

The results of the calculation are depicted in Fig. 3. These data were exploited for the evaluation of the anisotropic ratio AR curves (Fig. 4) with respect to the following relation

$$AR = \frac{\sigma_{n\,x}\left(L_y/W = L_z/W, \ L_x/W\right)}{\sigma_{n\,y,z}\left(L_x/W, L_y/W = L_z/W\right)}. \qquad (3)$$

The design procedure for the cube cross cell consists of the following steps:

1. For the desired anisotropic ratio, the relative dimensions of the arms size of the cross to the cube side (Lx/W, Ly/W, and Lz/W) should be selected with respect to Fig. 4. This choice is not unique since different combinations of relative dimensions can be found.
2. For the selected relative dimensions, the normalized effective electrical conductivity can be read from Fig. 3. Multiplying these values by the electrical conductivity of the inclusion, the resultant conductivities of the cell in principal directions are obtained.
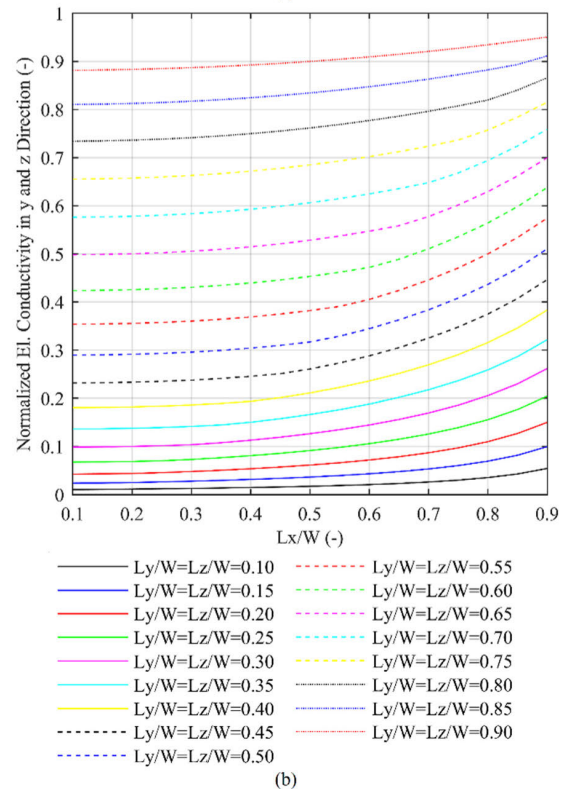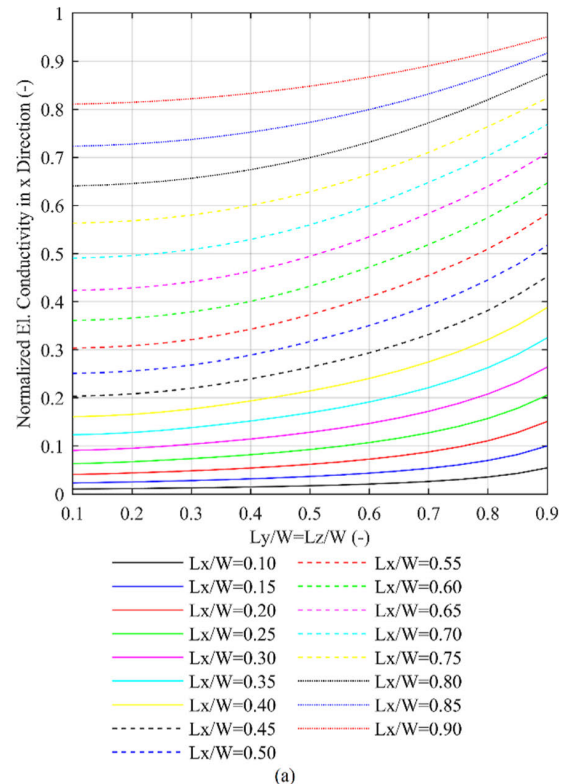

FIGURE 3. Evaluated normalized electrical conductivities in x direction (a), and in y and z direction (b) for different relative dimensions of the inclusion (Fig. 2).

3. Experimental verification of the designed cube cross cell parameters.

Note that the first step of the procedure should be done considering expected length of the cube side W, and the capability and accuracy of the fabrication process.

For the experimental verification, the agar mixture of desired conductivity should be prepared following the recommendation provided in [17]. Since the electrical conductivity of the agar mixture depends on the purity of used constituents, its values should be measured. For the proper filling of the space of the inclusion by an agar mixture, we recommend to heat up the measured structure up to the temperature of 60 °C if the temperature of the prepared agar mixture is about 80 °C. Instead of measuring a single cell, it is better to create a block of cells in the rectangular organization of $M \times N \times O$ cells. While filling the block with the agar mixture to get rid of air bubbles, it is appropriate to shake the block.

The white matter of our phantom (Fig. 1(c), (d)) will be approximated by a number of the cube cross cells to fill the space defined by the inverted-U shape. However, the white matter is surrounded by an isotropic medium of the conductivity of 0.33 S/m. To properly connect this medium with the white matter, we found it reasonable to mimic it by isotropic cube cross cells (all three arms have the same cross-section) surrounding the white matter. So the same procedure for the cube cross cell design can be exploited.

B. DESIGN ANISOTROPIC AND ISOTROPIC CELLS, FINAL COMPOSITION OF PHANTOM

To create the phantom, two kinds of cells have to be designed: anisotropic and isotropic. To assure matching anisotropic and isotropic part of the phantom, the inclusion of both these cells has to be realized by the same agar mixture. The design of those cells has to be a compromise between all the requirements. In addition, the capability and accuracy of the printing process have to be also considered. Since the agar mixture has to fill the cross shape of the inclusion we can expect troubles, e.g., not perfect filling the space of the inclusion by agar mixture, if the cube side of the cell or the inclusion dimensions are too small. Considering all of those facts we found that for the proper creation of the proposed phantom depicted in Fig. 2, the cube side is 4 mm. Further, considering the fact that the thickness of the white matter is about 0.4 mm, we are forced to scale the phantom by the factor 10. This is possible only for the linear operation regime of the phantom which has to be verified (Section IV, Fig. 10).

Based on the above consideration and the design procedure, which does not require any further exploitation of CST Studio Suite, and the recommendations in the previous section, we designed and measured properties of the anisotropic and isotropic cells and they are summarized in Table 1.

Note that the designed anisotropic cell corresponds with the requirements for the horizontal anisotropic layer of the inverted-U shape (Section II). The anisotropic cell for the vertical anisotropic layers of the inverted-U shape can be obtained by the rotation of that cell around y axis.

TABLE 1. Desired and measured properties of designed anisotropic and isotropic cells. Measured electrical conductivity of agar mixture is 1.56 S/m.

	Anisotropic cell				
	Lx (mm)	Ly (mm)	Lz (mm)	σ_{xx} (S/m)	$\sigma_{yy}=\sigma_{zz}$ (S/m)
Desired values	-	-	-	1.04	0.104
Measured values	3.55*	0.56*	0.56*	1.13	0.12
	Isotropic cell				
	$Lx=Ly=Lz$ (mm)			$\sigma_{xx}=\sigma_{yy}=\sigma_{zz}$ (S/m)	
Desired values	-			0.33	
Measured values	1.76*			0.33	

*The average measured dimensions of the cross.

C. PHANTOM FABRICATION

To fabricate the proposed anisotropic phantom (Fig. 5), the inner cell structure, composed from numerous anisotropic and isotropic cells, and the shell have to be printed. For the inner cell structure printing, we exploited the printer Original Prusa SL1 based on mask stereolithography (MSLA) technology and black resin [27]. Due to the big size of the phantom, the cell structure was divided into 6 parts and gradually printed (Fig. 6(a)).

The shell composed from a box and two lids for the inner cell structure was designed considering filling the cell

FIGURE 4. Evaluated anisotropic ratio with respect to equation (3).

structure by agar mixture from both directions allowing proper filling the space of the inverted-U shape white matter. These parts were printed (Fig. 6(b)) by an Original Prusa i3 MK3S based on fused filament fabrication (FFF) technology and polyethylene terephthalate glycol (PETG) filament [27].

To finalize the phantom, the following steps were carried out:

1. 5 holes were drilled to the printed inner cell structure for the excitation electric dipoles which models the neural activity of the brain. The dipoles whose surface was platinum plated are based on a coaxial line (Fig. 6(c)). The first arm of the dipole is created by a small cylinder which is pressed on the inner conductor of the coaxial cable. The second arm of the dipole is created by the bent outer conductor of the coaxial cable. The length of each dipole arm is 5 mm approximately, and the gap between the arms is 1.5 mm approximately. The diameter of the fabricated dipole is 5 mm.

2. 16 small holes were drilled for platinum plated electrodes [17]. These electrodes were fixed to a shell by a hot melt glue gun.

3. 6 parts of the printed inner cell structure were fixed to the box of the shell by a hot melt glue gun.

4. The fabricated structure was heated for 3 hours in a kiln at the temperature of 60 °C. In the meantime, 3.5 liters of agar mixture were prepared. After the preparation process, the agar mixture was gradually poured to the phantom. During this process, the phantom was shaken to get rid of air bubbles. The whole filling process took about half an hour.

5. The inner cell structure of the phantom was closed by two lids with the help of a hot melt glue gun and the
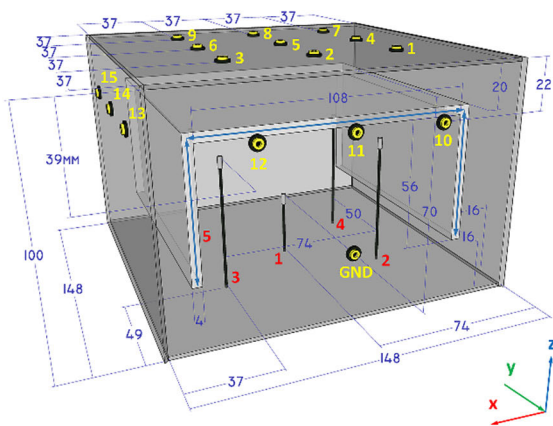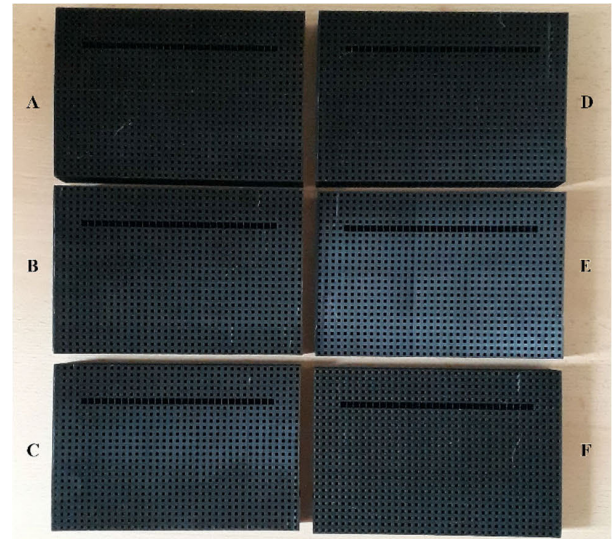

(a)

(b)

(c)

FIGURE 6. Inner cell structure divided into 6 parts (a), shell of phantom composed from a box and two lids (b), electric dipoles for modeling neural activity (c). The A and F part of the inner cell structure contains anisotropic cells (not seen in the figure) for approximation of vertical parts of anisotropic white matter.

FIGURE 5. Composition of the final anisotropic phantom. The three-dimensional inverted-U shape in white represents the anisotropic layer of the phantom which is approximated by numerous anisotropic cube cells. The space between the outer shell and the anisotropic layer is filled with isotropic cells (forming an isotropic material with conductivity of 0.33 S/m). The blue line terminated by arrows indicates tensors of the modelled anisotropy. Given dimensions are in millimeters. Electrodes are depicted in yellow colour with corresponding number labels (1-15 + ground electrode, GND). Dipoles are depicted as a black tail with a metal head, respective labels in red colour (1-5).

excitation dipoles were fixed to phantom by the same gun.

FIGURE 7. Fabricated anisotropic phantom.

The fabricated phantom depicted in Fig. 7 was cooled to room temperature for 18 hours and tested.

To investigate the influence of the anisotropic white matter on the source localization, an isotropic phantom (Fig. 8) was created in the same way with the following differences:

- The anisotropic white matter approximated by anisotropic cells at the anisotropic phantom was substituted by the isotropic cells.
- The box of the shell has a simple configuration, since the inverted-U profile is not considered and the phantom is filled by the agar mixture from one side.

IV. INFLUENCE OF ANISOTROPIC WHITE MATTER ON SOURCE LOCALIZATION

Generally, this section deals with a rather broad question, whether there is an effect of anisotropy on the Electrical
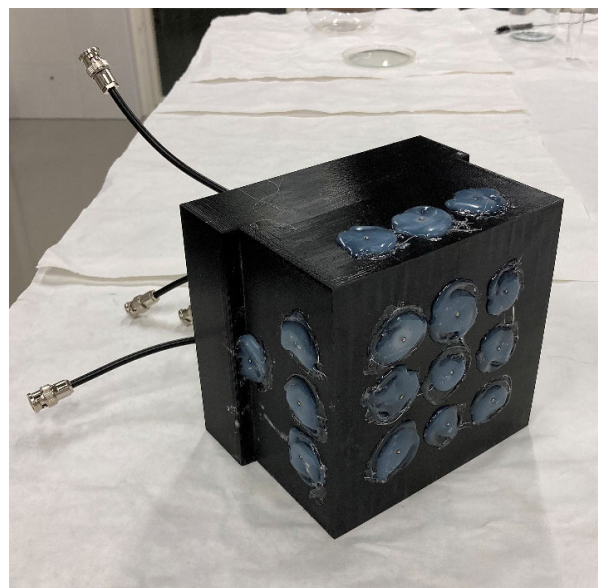

FIGURE 8. Fabricated isotropic phantom.

Source Imaging (ESI) and if there are any specific relations between the ESI changes and the spatial distribution of the anisotropic material. This question is addressed by testing of the two fabricated phantoms. Although this approach allows us to simulate a real EEG acquisition routine, the number of factors to be examined is naturally limited by the fabrication process. Specifically, a number of testing dipoles, orientation of the dipoles, a number of electrodes and their distribution, relative distances of the electrodes and dipoles from the anisotropic volume have to be fixed.

Thus, this section brings evidence to the question if there is a difference in the ESI between the isotropic and anisotropic conditions considering the simplified model of the rat head described above. In order to address the effect of different formulations of the source localization, two commonly used inverse solvers Exact Low Resolution Electromagnetic Tomography (ELORETA) [28] and Dynamical Imaging of Coherent Sources (DICS) [29] are utilized. The two conditions are compared in the terms of the single dipole localization errors and averaged localization error across all dipoles. Besides the dipole-wise localization error measurement, a voxel-wise similarity between the two conditions was evaluated across all dipoles. Thus, the two qualitatively different criteria, the error based and similarity based ones, are evaluated.

A. MATERIALS AND METHODS

The fabricated phantoms were tested in a similar way as it was done in our previous paper [17]. The five excitation dipoles were gradually connected to the generator TGF4042 AIM-TTI which provided a harmonic signal of frequency 1 kHz. The electrodes of the phantom were connected to BioSDA09, a standard 32-channel digital EEG amplifier (MI Ltd., Prague, Czech Republic), via a 16-lead cable (Data Sciences International, St. Paul, Minnesota, United States) connected to the electrodes by a dual-row IO socket connector. Sampling frequency was set to 5 kHz. The measurement workplace is depicted in Fig. 9.

Voltage between each sensing electrode and ground (GND) was measured. The transfer functions were calculated with the original GND reference. However, the recorded voltage was recalculated with respect to the average voltage across all sensing electrodes for the source localization procedure. The phantom measurements were provided in the same way as in the previous paper [17] up to input voltage amplitudes. Here, the input voltage was varied from 10 mV to 800 mV to measure the phantom transfer function on each dipole. Data for the localization procedure were recorded with 80 mV input signal amplitude within the linear regime of the phantom as depicted in Fig. 10.

Both isotropic and anisotropic volume conduction models were simulated utilizing the finite element method implemented in the Duneuro [30] library interfaced by the Brainstorm toolbox [31], which is documented and freely available for download online under the GNU general public license (http://neuroimage.usc.edu/brainstorm). Thus, both
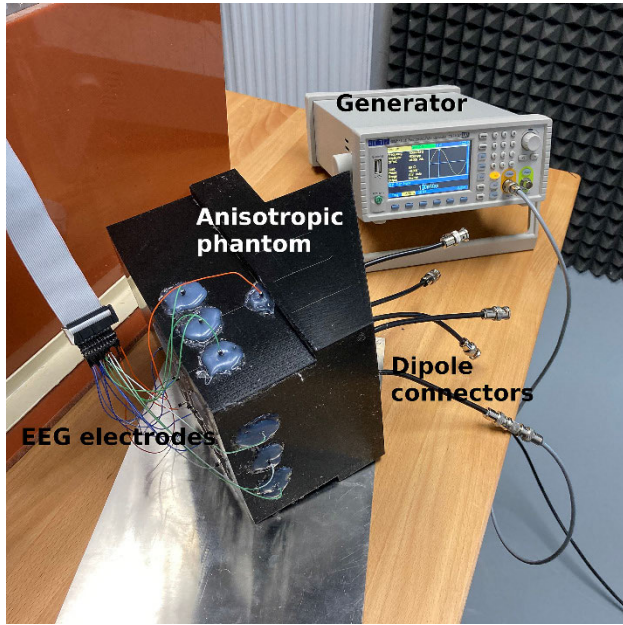
FIGURE 9. Experiment workplace for the anisotropic phantom measurement.

FIGURE 10. Measured electrode voltages at anisotropic rat head phantom for excitation dipole d2.

isotropic and anisotropic conditions were appropriately simulated. The phantom volume was discretized onto 288498 tetrahedrons. Electrodes were co-registered with the discretized phantom geometry, projected onto the phantom surface, and assigned to the closest node of the computational mesh. The source localization grid contained 52367 points which corresponded to the 4 millimeter spacing between surrounding solution points. For comparison, in our previous papers [32] and [17], 1557 and 2346 dipoles were used, respectively. Further increase of the grid density would lead to the dramatic increase of computational demands because a total number of source dipoles is proportional to the cube of a number of samples per direction. Regarding the implicit and inevitable smoothness of the inverse operator increase of sample density would not bring much more profit to the solutions.

Two eLORETA and DICS localization techniques were utilized in localization of the testing dipoles. Both methods were implemented in the fieldtrip toolbox [33]. For a more detailed description of both methods [32]. Since the DICS and eLORETA methods resulted in the very same localization errors on both phantoms, only the eLORETA results are reported here for the sake of brevity.

The true dipole positions in both fabricated phantoms were obtained from the computer tomography (CT) scan measured by the CT Siemens Somatom Definition Flash with the kind help of the CT department at the Institute for Clinical and Experimental Medicine in Prague. The CT image was co-registered with the computational model using ITK-SNAP software [25] such that the localization error could be enumerated. Further, all presented source estimation and volumetric data were interpolated and printed over the CT scan volume.
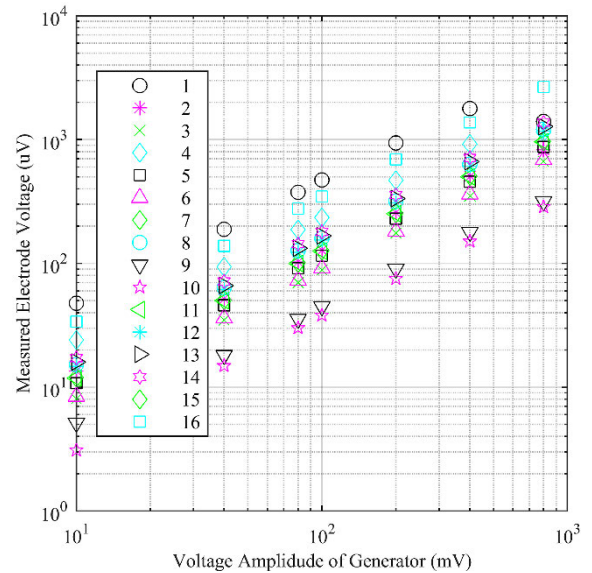
Measured average distances of dipoles d1, d2, d3, d4, and d5 from all electrodes were 87 mm, 80 mm, 67 mm, 90 mm, and 75 mm respectively.

The localization errors summarized in Table 2 were obtained by comparing the true dipole coordinates and coordinates of global maxima of estimated source distributions. Spatial distances between true and estimated dipole locations were computed in all principal axes separately. The root mean squared error (RMSE) across all dipoles was then enumerated. Finally, the Euclidean distance between the true and estimated locations was calculated.

The localization errors were computed for both isotropic (ISO) and anisotropic (ANI) forward solutions on both isotropic and anisotropic fabricated phantoms mimicking the white matter conductivity properties. The isotropic phantom measurement served as a control condition.

In order to assess the effect of neglecting anisotropy, the reliability map [34] across testing dipoles was computed in each voxel. More specifically, two solution vectors corresponding to ISO and ANI conditions $\hat{x}_i^{iso}$ and $\hat{x}_i^{ani}$ were computed for each i-th voxel. Each solution vector contained source estimates of all five testing dipoles. Each j-th dipole measurement was considered as a testing function for calculating the reliability of neglecting anisotropic properties of the phantom by using an isotropic forward model. The reliability metric between the two vectors was calculated in each i-th voxel such that a reliability map was obtained [34] as follows:

$$reliability_i = \sum_{j=1}^{nDip} \frac{\left| \frac{\hat{x}_{i,j}^{iso}}{\left\| \hat{x}_{i,j}^{iso} \right\|} - \frac{\hat{x}_{i,j}^{ani}}{\left\| \hat{x}_{i,j}^{ani} \right\|} \right| \cdot \frac{\left\| \hat{x}_{i,j}^{ani} \right\|}{\max_{i \in V} \left(\left| \hat{x}_{i,j}^{ani} \right| \right)}}{nDip}, \quad (4)$$

where the $\hat{x}_{i,j}$ is the source estimation in the i-th voxel corresponding to the excitation of the j-dipole, the $nDip$ is a

number of testing dipoles, the V is a set of all voxel indices, the || and ‖ ‖ are the absolute value and L2 operators, respectively.

B. RESULTS

In Table 2, the ISO and ANI conditions are compared in terms of localization error. The first part of Table 2 "Anisotropic phantom" corresponds to measurement on anisotropic phantom while the second part "Isotropic phantom" summarizes errors measured on isotropic phantom. Clearly, the highest error can be observed in the z direction, which is due to the depth bias caused by superficial distribution of the electrodes. Generally, the measured errors are very similar between ISO and ANI conditions in both anisotropic and isotropic phantoms. The key results are summarized in the first part of Table 2 where we answer how the localization error is changed in ISO condition (neglected anisotropy of white matter) with respect to ANI condition (involved anisotropy of white matter) if the measured phantom is anisotropic. A decreased error by 7 mm in the ANI condition in anisotropic phantom was observed for dipole d3 with respect to the ISO condition. The higher accuracy was mostly pronounced in Z direction. In the case of isotropic phantom, there was also a decreased error specifically for the dipole d3 which is further discussed in the next section. In Fig. 11, estimated source distributions for the d3 dipole utilizing ISO and ANI forward models in anisotropic phantom are compared.

In Fig. 12, the reliability map is depicted. The reliability map estimates spatial distribution of source reconstruction errors due to neglecting anisotropy. The orthogonal slices intersect positions of two selected dipoles d1 and d3 in Fig. 12(a) and Fig. 12(b) respectively. The reliability is spatially structured and related to the shape of the anisotropic compartment. The error is mostly pronounced in the vicinity of the anisotropic compartment and in the area surrounded by the anisotropic compartment.

C. DISCUSSION ON THE EFFECT OF ANISOTROPY

The dipole-wise errors summarized in Table 2 reached similar values between ISO and ANI conditions. In case of measurement on the anisotropic phantom, the effect of neglecting anisotropy on localization error was addressed. The results answer the question if the isotropic approximation is appropriate to localize sources embedded in an anisotropic volume conductor. Most of the measured error differences were smaller than the spatial spacing in the solution grid. Thus, we conclude that the effect of anisotropy on a single dipole localization was not observed in our phantom experiment. This is in correspondence with both simulation and experimental studies, where changes in dipole amplitude rather than changes in dipole positions were reported as an observed effect of anisotropy [7], [8], and [35]. In the case of measurement on the isotropic phantom, the effect of wrongly applied anisotropic solver to the isotropic problem on the source localization error was addressed. Again, source reconstruction errors compared between anisotropic and isotropic

phantoms reached similar values and the differences were below the resolution of the solution grid.

It is worthy to mention that increased localization error due to neglecting anisotropy was observed specifically on the d3 testing dipole. The d3 dipole had the smallest averaged distance from all electrodes. This result can be explained by a concentrated sensitivity of the electrode system to the dipole sources within the phantom volume surrounded by electrodes [36]. The more concentrated sensitivity can allow more precise localization when anisotropy is involved in the model. However, since the error decreased also in the case of the isotropic phantom, when the true forward model was isotropic, we conclude that this phenomenon is not explained by the factor of anisotropy.

TABLE 2. Error of source localization technique in case of single dipole excitation.

	x (mm)		y (mm)		Z (mm)		Euclidean (mm)	
Anisotropic phantom								
*forward model**	ISO	ANI	ISO	ANI	ISO	ANI	ISO	ANI
d1	5	5	7	7	69	69	70	70
d2	22	22	-11	-11	37	37	44	44
d3	-20	-16	-10	-14	37	21	43	30
d4	18	18	8	8	36	36	41	41
d5	-17	-17	12	12	21	21	30	30
rmse⁺	17	17	10	11	43	41	47	45
Isotropic phantom								
	x (mm)		y (mm)		z (mm)		Euclidean (mm)	
*forward model**	ISO	ANI	ISO	ANI	ISO	ANI	ISO	ANI
d1	5	5	8	8	68	68	69	69
d2	18	14	-9	-13	30	30	36	36
d3	-19	-11	-8	-12	26	22	33	27
d4	18	18	10	10	38	38	43	43
d5	-15	-11	9	13	18	22	25	28
rmse⁺	16	13	9	11	40	40	44	43

*The ISO and ANI denotes isotropic and anisotropic forward solvers, respectively.
⁺Root mean squared error across all dipoles.

Strong correlation between ISO and ANI errors across testing dipoles can be clearly observed in Table 2. Thus, we conclude that the dipole position with respect to the electrodes had a strong effect on the localization error in our experiment.

The obtained solutions of the inverse localization problem contained clear, so called, depth bias. In other words, the main error component was in the Z direction. This was mainly due to rather superficial electrode displacement. The electrodes should ideally cover all walls of the phantom. The ideal displacement is not the case of real experiments both in humans and animals. The goal of this study was to approximate a real in vivo experimental setup in rats and to mimic the effect of white matter which led to the observed errors. Our experiment was limited to the asymmetrical placement of the electrodes due to the complexity of the anisotropic phantom fabrication. In this way, the approximation deviated from a common
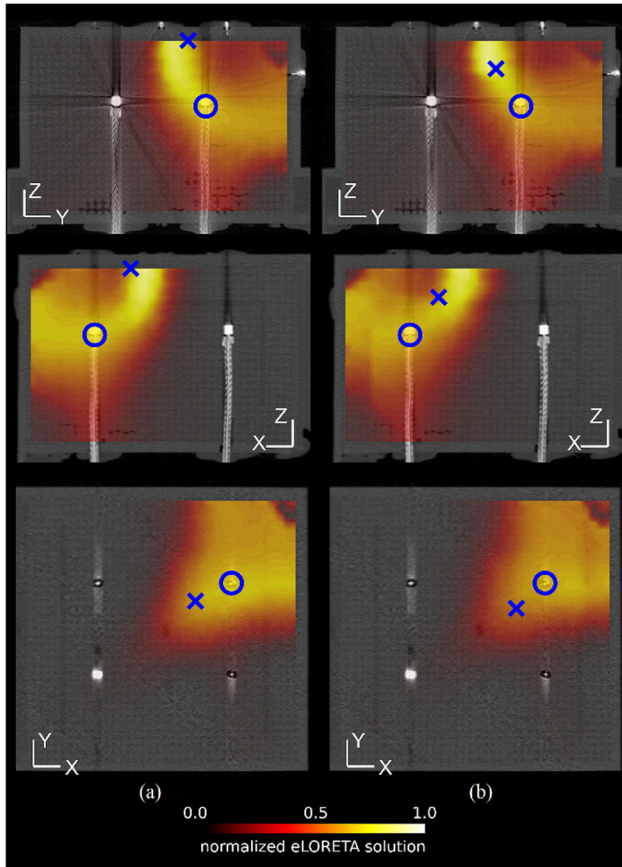
FIGURE 11. Comparison of the isotropic-ISO (A) and anisotropic-ANI (B) forward solutions used for source reconstructions of the d3 dipole measured on the anisotropic phantom. The true position of the d3 testing dipole is marked with a blue circle, the maximum of the eLORETA solution is marked with a blue cross. Three depicted orthogonal planes intersect at the position of the d3 dipole.

FIGURE 12. The source reconstruction error map of the isotropic forward solution with respect to anisotropic solution. Slices intersection point is chosen at the d1 (A) and d3 (B) dipole positions. All dipole positions are marked with blue markers: d1 ('x'), d2 ('o'), d3 ('square'), d4 ('diamond'), and d5 ('+').

symmetrical electrode setup in real experiments. However, since the problem was geometrically symmetric, the results are still valid for a certain degree of generalization.

The depth bias induced by our electrode displacement was simulated by the FEM method considering both homogeneous isotropic and anisotropic models (not presented in the paper). It is worthy to mention that the same bias of the eLORETA reconstruction was observed independently of the phantom fabrication.

It is also of importance to map the effects of neglecting anisotropy to the regions distant from the actual testing dipole positions. This is essential for avoiding false positive activation findings and for, so-called, functional connectivity calculation between two distant brain regions. The functional connectivity is commonly calculated as a correlation of two signal envelopes between two voxels. Spread spurious EEG sources estimations due to neglecting anisotropy (Fig. 12) can lead to spurious correlation of signal envelopes. To the best of our knowledge, all of the past studies have reported effects of neglecting anisotropy on source reconstruction of a single dipole under the test. To assess the voxel-wise similarity, a reliability map representing source localization differences within the entire brain model due to anisotropy considering
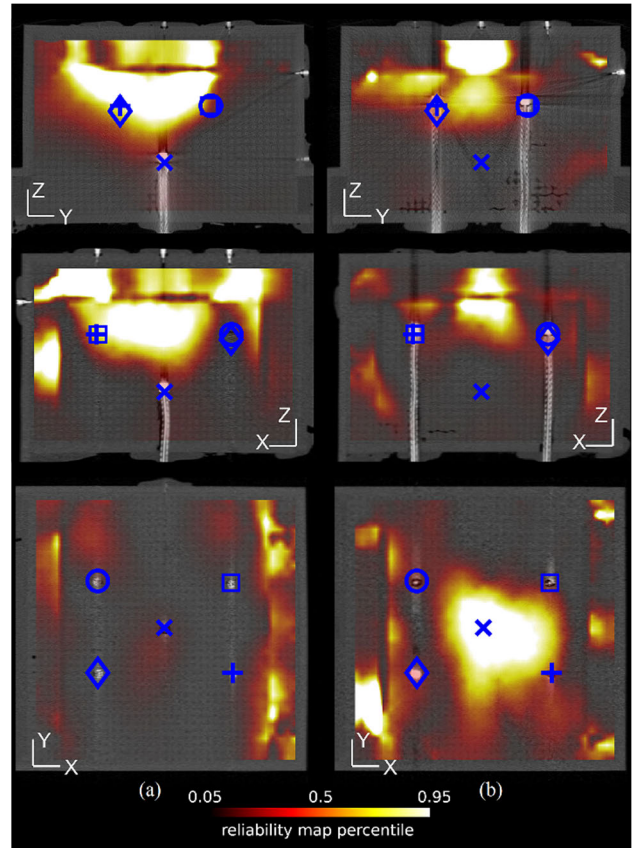
five testing dipoles was calculated. Increased error values were observed in areas close to the electrodes where the most energy of the solution is concentrated. However, increased error was clearly observed in the vicinity of the anisotropic compartment mimicking the white matter even in those areas distant from the electrodes. This is in correspondence with previous simulation-based studies. Thus, our results increase evidence and provide experimental validation of the previous hypothesis that sources in the vicinity of the anisotropic volume conductors are the most influenced ones.

V. CONCLUSION

In this paper we introduced a design procedure for the anisotropic rat head phantom which can be fabricated with currently available conventional techniques. It is based on the cubic cross cell composition combined with agar mixture to set desired electrical conductivity anisotropic ratio. The proposed procedure was designed for the design and fabrication of anisotropic and isotropic phantoms.

The effect of anisotropy to the ESI was measured and computed on those two phantoms. There was a weak effect of anisotropy on dipole localization error. A reliability map was computed and interpreted to study spatial differences between ISO and ANI source reconstructions. The highest differences

were observed in the areas close to the electrodes and in the areas in the vicinity of the anisotropic compartments.

REFERENCES

[1] H. Hallez, B. Vanrumste, R. Grech, J. Muscat, W. De Clercq, A. Vergult, Y. D'Asseler, K. P. Camilleri, S. G. Fabri, S. Van Huffel, and I. Lemahieu, "Review on solving the forward problem in EEG source analysis," *J. NeuroEng. Rehabil.*, vol. 4, no. 1, Nov. 2007, Art. no. 46.

[2] P. W. Nicholson, "Specific impedance of cerebral white matter," *Exp. Neurol.*, vol. 13, no. 4, pp. 386–401, 1965.

[3] G. Marin, C. Guerin, S. Baillet, L. Garnero, and G. Meunier, "Influence of skull anisotropy for the forward and inverse problem in EEG: Simulation studies using FEM on realistic head models," *Hum. Brain Mapping*, vol. 6, no. 4, pp. 250–269, 1998.

[4] T. Goto, R. Hatanaka, T. Ogawa, A. Sumiyoshi, J. Riera, and R. Kawashima, "An evaluation of the conductivity profile in the somatosensory barrel cortex of Wistar rats," *J. Neurophysiol.*, vol. 104, no. 6, pp. 3388–3412, Dec. 2010.

[5] C. H. Wolters, A. Anwander, X. Tricoche, D. Weinstein, M. A. Koch, and R. MacLeod, "Influence of tissue conductivity anisotropy on EEG/MEG eld and return current computation in a realistic head model: A simulation and visualization study using high-resolution finite element modeling," *NeuroImage*, vol. 30, no. 3, pp. 813–826, 2006.

[6] V. Montes-Restrepo, P. van Mierlo, G. Strobbe, S. Staelens, S. Vandenberghe, and H. Hallez, "Influence of skull modeling approaches on EEG source localization," *Brain Topogr.*, vol. 27, no. 1, pp. 95–111, Jan. 2014.

[7] D. Güllmar, J. Haueisen, M. Eiselt, and F. Gieβler, "Influence of anisotropic conductivity on EEG source reconstruction: Investigations in a rabbit model," *IEEE Trans. Biomed. Eng.*, vol. 53, no. 9, pp. 1841–1850, Sep. 2006.

[8] D. Güllmar, J. Haueisen, and J. R. Reichenbach, "Influence of anisotropic electrical conductivity in white matter tissue on the EEG/MEG forward and inverse solution. A high-resolution whole head simulation study," *NeuroImage*, vol. 51, no. 1, pp. 63–145, May 2010.

[9] H. Hallez, B. Vanrumste, P. Van Hese, S. Delputte, and I. Lemahieu, "Dipole estimation errors due to differences in modeling anisotropic conductivities in realistic head models for EEG source analysis," *Phys. Med. Biol.*, vol. 53, no. 7, pp. 1877–1894, Apr. 2008.

[10] N. Samadzadehaghdam, B. MakkiAbadi, and S. Masjoodi, "Evaluating the impact of white matter conductivity anisotropy on reconstructing eeg sources by linearly constrained minimum variance beamformer," *Adv. Biomed. Eng.*, vol. 9, pp. 53–61, Oct. 2020.

[11] W. H. Lee, Z. Liu, B. A. Mueller, K. Lim, and B. He, "Influence of white matter anisotropic conductivity on EEG source localization: Comparison to fMRI in human primary visual cortex," *Clin. Neurophysiol.*, vol. 120, no. 12, pp. 2071–2081, Dec. 2009.

[12] R. J. Cooper, R. Eames, J. Brunker, L. C. Enfield, A. P. Gibson, and J. C. Hebden, "A tissue equivalent phantom for simultaneous near-infrared optical tomography and EEG," *Biomed. Opt. Exp.*, vol. 1, no. 2, pp. 425–430, 2010.

[13] R. M. Leahy, J. C. Mosher, M. E. Spencer, M. X. Huang, and J. D. Lewine, "A study of dipole localization accuracy forMEG and EEG using a human skull phantom," *Electroencephalogr. Clin. Neurophysiol.*, vol. 107, no. 2, pp. 159–173, 1998.

[14] T. J. Collier, D. B. Kynor, J. Bieszczad, W. E. Audette, E. J. Kobylarz, and S. G. Diamond, "Creation of a human head phantom for testing of electroencephalography equipment and techniques," *EEE Trans. Biomed. Eng.*, vol. 59. no. 9, pp. 2628–2634, Sep. 2012.

[15] H. Yang and H. Jiang, "Design and evaluation of a miniature probe integrating diffuse optical tomography and electroencephalographic source localization," *Appl. Opt.*, vol. 52, no. 20, pp. 5036–5041, Jul. 2013.

[16] D. Kim, J. Jeong, S. Jeong, S. Kim, S. C. Jun, and E. Chung, "Validation of computational studies for electrical brain stimulation with phantom head experiments," *Brain Stimulation*, vol. 8, no. 5, pp. 914–925, 2015.

[17] J. Lacik, V. Koudelka, D. Kuratko, Z. Raida, D. K. Wojcik, T. Mikulasek, J. Vanek, S. Jiricek, and C. Vejmola, "Rat head phantom for testing of electroencephalogram source localization techniques," *IEEE Access*, vol. 8, pp. 106735–106745, 2020.

[18] E. Tsizin, T. Mund, and A. Bronstein, "Printable anisotropic phantom for EEG with distributed current sources," in *Proc. IEEE Int. Symp. Biomed. Imag. (ISBI)*, Washington, DC, USA, Apr. 2018, pp. 4–7.

[19] S. Liang, S. Wu, Q. Huang, S. Duan, H. Liu, and Y. Li, "Rat brain digital stereotaxic white matter atlas with fine tract delineation in Paxinos space and its automated applications in DTI data analysis," *Magn. Reson. Imag.*, vol. 43, pp. 122–128, Oct. 2017.

[20] P. J. Basser, J. Mattiello, and D. Lebihan, "Estimation of the effective self-diffusion tensor from the NMR spin echo," *J. Magn. Reson., B*, vol. 103, no. 3, pp. 247–254, Mar. 1994.

[21] S. Mori and P. C. M. Van Zijl, "Fiber tracking: Principles and strategies—A technical review," *NMR Biomed.*, vol. 15, nos. 7–8, pp. 468–480, 2002.

[22] L. M. Alba-Ferrara and G. A. de Erausquin, "What does anisotropy measure? Insights from increased and decreased anisotropy in selective fiber tracts in schizophrenia," *Frontiers Integr. Neurosci.*, vol. 7, pp. 1–5, Feb. 2013.

[23] G. A. Johnson, E. Calabrese, A. Badea, G. Paxinos, and C. Watson, "A multidimensional magnetic resonance histology atlas of the Wistar rat brain," *NeuroImage*, vol. 62, no. 3, pp. 1848–1856, 2012.

[24] A. Rumple, M. McMurray, J. Johns, J. Lauder, and P. Makam, "3-dimensional diffusion tensor imaging (DTI) atlas of the rat brain," *PLoS ONE*, vol. 8, no. 7, 2013, Art. no. e67334.

[25] P. A. Yushkevich, J. Piven, H. Hazlett, and R. Smith, "User-guided 3D active contour segmentation of anatomical structures: Significantly improved efficiency and reliability," *NeuroImage*, vol. 31, no. 3, pp. 1116–1128, Jul. 2006.

[26] B. Guru and H. Hiziroglu, *Electromagnetic Field Theory and Fundamentals*. Cambridge, U.K.: Cambridge Univ. Press, 2004.

[27] Prusa Research. *Prague, Czech Republic*. Accessed: Aug. 10, 2021. [Online]. Available: https://www.prusa3d.com/

[28] R. Pascual-Marqui and D. Lehmann, "Assessing interactions in the brain with exact low-resolution electromagnetic tomography," *Philos. Trans. A, Math. Phys. Eng. Sci.*, vol. 369, no. 1952, pp. 3768–3784, 2011.

[29] J. Gross, J. Kujala, M. Hämäläinen, L. Timmermann, A. Schnitzler, and R. Salmelin, "Dynamic imaging of coherent sources: Studying neural interactions in the human brain," *Proc. Nat. Acad. Sci. USA*, vol. 98, no. 2, pp. 694–699, 2001.

[30] S. Schrader, A. Westhoff, M. Piastra, and T. Miinalainen, "DUNEuro—A software toolbox for forward modeling in bioelectromagnetism," *PLoS ONE*, vol. 16, no. 6, Jun. 2021, Art. no. e0252431.

[31] F. Tadel, S. Baillet, J. C. Mosher, D. Pantazis, and R. M. Leahy, "Brainstorm: A user-friendly application for MEG/EEG analysis," *Comput. Intell. Neurosci.*, vol. 2011, pp. 1–13, Oct. 2011.

[32] S. Jiricek, V. Koudelka, J. Lacik, C. Vejmola, D. Kuratko, D. K. Wójcik, Z. Raida, J. Hlinka, and T. Palenicek, "Electrical source imaging in freely moving rats: Evaluation of a 12-electrode cortical electroencephalography system," *Frontiers Neuroinform.*, vol. 14, p. 68, Jan. 2021.

[33] R. Oostenveld, P. Fries, E. Maris, and J.-M. Schoffelen, "FieldTrip: Open source software for advanced analysis of MEG, EEG, and invasive electrophysiological data," *Comput. Intell. Neurosci.*, vol. 2011, pp. 1–9, May 2011.

[34] C. Chintaluri, M. Kowalska, W. Sredniawa, M. Czerwinski, J. M. Dzik, J. Jedrzejewska-Szmek, and D. K. Wójcik, "kCSD-python, a tool for reliable current source density estimation," *bioRxiv*, p. 708511, Jul. 2019.

[35] J. Haueisen, D. S. Tuch, C. Ramon, P. H. Schimpf, V. J. Wedeen, J. S. George, and J. W. Belliveau, "The influence of brain tissue anisotropy on human EEG and MEG," *NeuroImage*, vol. 15, no. 1, pp. 159–166, Jan. 2002.

[36] J. Malmivuo, V. Suihko, and H. Eskola, "Sensitivity distributions of EEG and MEG measurements," *IEEE Trans. Biomed. Eng.*, vol. 44, no. 3, pp. 196–208, Mar. 1997.

JAROSLAV LACIK (Member, IEEE) received the M.Sc. and Ph.D. degrees from the Brno University of Technology, Brno, Czech Republic, in 2002 and 2007, respectively. He is currently an Associate Professor with the Brno University of Technology. His research interests include antennas, body-centric wireless communication, computational electromagnetics, and measurement.
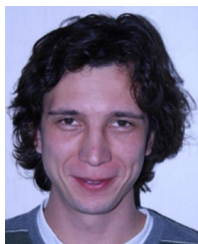
VLASTIMIL KOUDELKA was born in Usti nad Labem, Czech Republic. He received the M.Sc. and Ph.D. degrees from the Brno University of Technology, in 2009 and 2014, respectively. He is currently a Senior Researcher with the Institute of Mental Health, Klecany. His research interests include analysis and integration of neuroimaging data, machine learning, and signal synchronization in multimodal signal acquisition.

CESTMIR VEJMOLA received the M.Sc. degree from the Faculty of Science, Charles University, Prague. He is currently pursuing the master's degree with the National Institute of Mental Health, Klecany. His research interests include translational neuroscience, animal models of mental diseases, electrophysiology, and bioelectronics.

DAVID KURATKO received the M.Sc. degree from the Department of Radio Electronics, Faculty of Electrical Engineering and Communication, Brno University of Technology (FEEC—BUT), in 2018, where he is currently pursuing the Ph.D. degree with the Department of Radio Electronics. His research interest includes the rat's head forward modeling.

JIRI VANEK received the Ph.D. degree from the Brno University of Technology, Brno, Czech Republic, in 2004. He is currently an Associate Professor with the Department of Electrical and Electronic Technology, Faculty of Electrical Engineering and Communication, Brno University of Technology. His research interests include diagnostics methods of materials properties, technology and design of, photovoltaic, and other renewable sources of energies.
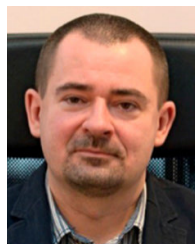
DANIEL KRZYSZTOF WÓJCIK received the M.Sc. and Ph.D. degrees from the Department of Physics, University of Warsaw, in 1996 and 2000, respectively. He was a Research Assistant with the Center for Theoretical Physics PAS, from 1996 to 2000. He worked with the Institute for Physical Science and Technology, University of Maryland, from 2000 to 2002, and the School of Physics, from 2002 to 2003, on deterministic models of quantum walks which formed the basis of his habilitation, Institute of Physics PAS, in 2008. In 2003, he joined the Nencki Institute of Experimental Biology PAS, where he is currently a Professor and the heads of the Laboratory of Neuroinformatics. Since 2019, he has been runs the Neuro Group within the Bioinspired Artificial Neural Networks Consortium at Jagiellonian University. He is also an Adjunct Research Professor with the Technical University of Brno.

TOMAS PALENICEK received the M.D. and Ph.D. degrees from the 3rd Faculty of Medicine, Charles University, Prague, in 2001 and 2009, respectively. He is currently a leading Senior Scientist in the psychedelic research and the Translational EEG with the National Institute of Mental Health, Czech Republic. His research interests include neuroimaging and translational research with psychedelics, such as psilocybin, LSD, 2C-B, and on MDMA. He is currently a Principal Investigator of several clinical trials investigating effects of psychedelics in healthy volunteers and in patients suffering depression with exploratory measures focusing on the underlying neurobiology using neuroimaging methods.

ZBYNEK RAIDA (Senior Member, IEEE) received the M.Sc. and Ph.D. degrees from the Brno University of Technology (BUT), in 1991 and 1994, respectively. He is currently a Professor at BUT. His research interests include applied electromagnetics, computational electromagnetics, and exploitation of artificial intelligence techniques for electromagnetic design.

• • •